


Please cite the Published Version

Aziz, Alex , Yu, Wei, Tang, Rui, Crespo-Otero, Rachel, Tommaso, Devis Di and Nishihara, Hiro-tomo (2024) Theoretical insights into the role of defects in the optimization of the electrochemical capacitance of graphene. *Energy Materials and Devices*, 2 (3). 9370035 ISSN 3005-3315

DOI: <https://doi.org/10.26599/emd.2024.9370035>

Publisher: Tsinghua University Press

Version: Published Version

Downloaded from: <https://e-space.mmu.ac.uk/636950/>

Usage rights:  [Creative Commons: Attribution 4.0](https://creativecommons.org/licenses/by/4.0/)

Additional Information: This is an open access article which first appeared in *Energy Materials and Devices*

Enquiries:

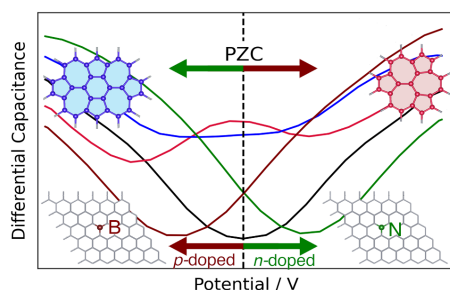
If you have questions about this document, contact openresearch@mmu.ac.uk. Please include the URL of the record in e-space. If you believe that your, or a third party's rights have been compromised through this document please see our Take Down policy (available from <https://www.mmu.ac.uk/library/using-the-library/policies-and-guidelines>)

Research Article


Theoretical insights into the role of defects in the optimization of the electrochemical capacitance of graphene

Alex Aziz , Wei Yu, Rui Tang, Rachel Crespo-Otero, Devis Di Tommaso, and Hirotomo Nishihara 

Graphical Abstract



Assessing the effects of structural defects and substitutional doping on the potential of zero charge (PZC) and capacitance curves of graphene using joint density functional theory.

 Address correspondence to Alex Aziz, a.aziz@mmu.ac.uk; Hirotomo Nishihara, hirotomo.nishihara.b1@tohoku.ac.jp

Received: January 26, 2024

Revised: May 2, 2024

Accepted: May 7, 2024

 Read Online

 Submit Online

Citation: Aziz A., Yu W., Tang R., et al. Theoretical insights into the role of defects in the optimization of the electrochemical capacitance of graphene. *Energy Mater. Devices*, 2024, 2(3), 9370035. <https://doi.org/10.26599/EMD.2024.9370035>

Theoretical insights into the role of defects in the optimization of the electrochemical capacitance of graphene

Alex Aziz¹ ✉, Wei Yu², Rui Tang³, Rachel Crespo-Otero⁴, Devis Di Tommaso⁵, and Hiroto Nishihara^{2,6} ✉

¹ Manchester Metropolitan University, Department of Natural Sciences, Manchester M1 5GD, United Kingdom

² Advanced Institute for Materials Research (WPI-AIMR), Tohoku University, Sendai 980-8577, Japan

³ College of Materials Science and Engineering, Hunan Joint International Laboratory of Advanced Materials and Technology for Clean Energy, Hunan Province Key Laboratory for Advanced Carbon Materials and Applied Technology, Hunan University, Changsha 410082, China

⁴ Department of Chemistry, University College London, London WC1H 0AJ, United Kingdom

⁵ Department of Chemistry, School of Physical and Chemical Sciences, Queen Mary University of London, London E1 4NS, United Kingdom

⁶ Institute of Multidisciplinary Research for Advanced Materials, Tohoku University, Sendai 980-8577, Japan

Received: January 26, 2024 / Revised: May 2, 2024 / Accepted: May 7, 2024

ABSTRACT

Graphene-based frameworks suffer from a low quantum capacitance due to graphene's Dirac point at the Fermi level. This theoretical study investigated the effect structural defects, nitrogen and boron doping, and surface epoxy/hydroxy groups have on the electronic structure and capacitance of graphene. Density functional theory calculations reveal that the lowest energy configurations for nitrogen or boron substitutional doping occur when the dopant atoms are segregated. This elucidates why the magnetic transition for nitrogen doping is experimentally only observed at higher doping levels. We also highlight that the lowest energy configuration for a single vacancy defect is magnetic. Joint density functional theory calculations show that the fixed band approximation becomes increasingly inaccurate for electrolytes with lower dielectric constants. The introduction of structural defects rather than nitrogen or boron substitutional doping, or the introduction of adatoms leads to the largest increase in density of states and capacitance around graphene's Dirac point. However, the presence of adatoms or substitutional doping leads to a larger shift of the potential of zero charge away from graphene's Dirac point.

KEYWORDS

implicit solvent models, electrical double layer, joint density functional theory, graphene based supercapacitors, quantum capacitance

1 Introduction

Renewable energy generation is at the cornerstone of efforts to combat climate change and the move to a carbon-neutral society. The increased frequency of extreme weather events and the recent accelerated governmental motivation due to geopolitics and energy security, has led to the increased implementation of renewable energy technology such as solar and wind. However, renewable energy generation

remains somewhat unpredictable and intermittent, being dependent on atmospheric and climatic conditions. To mitigate this energy storage methods are critical for the move to a carbon net-zero economy^[1]. Supercapacitors are advantageous over conventional rechargeable batteries where short-term power is required, for example for electrical grid stabilization or regenerative braking, due to their superior power density as well as their increased cyclability and ther-

✉ Address correspondence to Alex Aziz, a.aziz@mmu.ac.uk; Hiroto Nishihara, hirotomo.nishihara.b1@tohoku.ac.jp

© The Author(s) 2024. Published by Tsinghua University Press. The articles published in this open access journal are distributed under the terms of the Creative Commons Attribution 4.0 International License (<http://creativecommons.org/licenses/by/4.0/>), which permits use, distribution and reproduction in any medium, provided the original work is properly cited.

mal stability^[2], but they do suffer from low energy densities^[3,4]. Depending on the charge storage mechanism supercapacitors can be divided into three groups: an electrical double layer (EDL) capacitor where the charge is stored electrostatically; a pseudocapacitor, where charge is stored via fast redox reactions; or a hybrid capacitor using EDL and redox reaction across its two electrodes^[5]. Carbon-based EDL capacitors store energy by forming an EDL upon charging and discharging. As charge storage is electrostatic (rather than via electrochemical reactions), they exhibit excellent cyclability and capacity retention but low energy densities. But multi-layered carbon-based materials offer limited accessible surface area for energy storage. In the search for materials with a larger capacitance and thus energy density, one approach has been to introduce spacers between carbon layers thereby increasing the accessible surface area. An alternative approach has been to produce aqueous dispersions of holey graphene oxides and subsequent fabrication of hydrogels with improved specific surface areas^[6]. In defect-rich graphene-based electrodes such as reduced graphene oxides, which may be beneficial for ion adsorption, conductivities are significantly reduced. One approach to mitigate this challenge is hybridization with conductive noble metals or the addition of metal nanoparticles^[7]. An alternative approach has been the investigation highly porous carbons consisting of minimally stacked graphene frameworks that exhibit exceptionally large surface areas^[3,8-13]. Intrinsically, EDL capacitors based on graphene frameworks suffer from a low number of available electronic density of states (DOS) around the Fermi level that leads to a limited quantum capacitance (C_Q). This limits their overall total capacitance (C_{tot})^[8,14-17], as C_{tot} is comprised of C_Q and a non-quantum capacitance (C_{NQ}), arranged in series and thereby related through an inverse sum. This limited capacitance manifests itself through butterfly shaped cyclic voltammetry curves^[18]. As this work deals with single layer graphene frameworks there is no dielectric capacitance contribution to C_{NQ} ; and C_{NQ} is equal to the EDL capacitance (C_{EDL})^[15].

$$\frac{1}{C_{\text{tot}}} = \frac{1}{C_{\text{EDL}}} + \frac{1}{C_Q} \quad (1)$$

where C_Q is formally defined as

$$C_Q = \frac{d\sigma}{dV_Q} \quad (2)$$

Here $d\sigma$ is the change in surface charge density and dV_Q is the change in chemical potential ($-\mu/e$) as electrons are added or removed from the system, often referred to as the differential capacitance^[19]. The negative sign accounts for the transition from an energy to a potential scale and e is the elementary

charge of the electron^[14]. Or alternatively, C_Q can be expressed as a function of the electronic density of states

$$C_Q = e^2 \frac{n(\mu, N)}{1 - \int_{-\infty}^{\mu(N)} \frac{\delta n(E, N)}{\delta N} dE} \quad (3)$$

where $n(\mu, N)$ is the number of DOS as a function of the chemical potential (μ) and the number (N) of electrons per unit area deviating from the neutral system. The integral on the denominator represents the change in the DOS as a function of excess charge. When the change in DOS is neglected, the integral in the denominator of Eq.(3) is 0, and this leads to the fixed band approximation (FBA). The FBA does not take into account changes in the DOS due to structural changes on the addition or removal of electrons^[14]. Furthermore, the FBA does not consider changes in the DOS due to the re-distribution of charge carriers at the interface as the potential is varied. Whilst this approximation may hold at small changes in charge (or potential)^[14], for larger deviations it may prove necessary to consider the change in the DOS as well as the charge redistribution at the electrode surface in the presence of the EDL. This has been suggested to lead to more consistent agreement between computation and experiment for graphene^[14]. Over the past decade several strategies have emerged to estimate the EDL capacitance using a variety of computational models, although some of these methods are still underdeveloped and may exhibit erroneous results^[20,21]. The most accurate method involves computationally intensive explicit *ab initio* molecular dynamic (AIMD) calculations that require the sampling of thousands of configurations to obtain the necessary statistics to assess the electronic properties of liquids. As a trade-off between accuracy and computational efficiency, implicit solvent models that mimic the presence of the solvent in an average manner have become increasingly utilized (Fig. 1).

This approach has been implemented in several studies using the joint density functional theory (JDFT)^[22] to determine C_{tot} and highlight the limited C_Q around the Fermi level in graphene-based materials^[14-16,23]. Other experimental and theoretical studies have focused on increasing the number of electronic states around the Fermi level, with the inclusion of structural vacancy defects^[9,24], doping with nitrogen^[25] or boron^[26,27], or the addition of adatoms on the graphene surface^[28]. This is of particular importance to the recently fabricated edge-free carbon frameworks, which have shown higher stability, thereby allowing for high operating voltages^[29,30]. In this work we employ JDFT to undertake a theoretical study on the effect that structural vacancy defects^[31], nitrogen and boron substitutional doping, and the addition

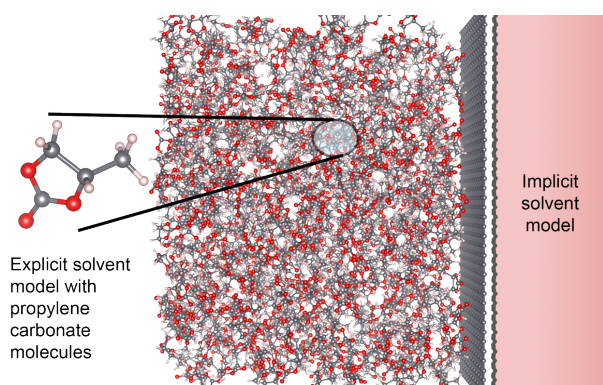


Figure 1 Model of a graphene surface solvated using explicit propylene carbonate molecules (left) and right a schematic representation of an implicit solvent used to model its average properties (this work).

that surface epoxy, or hydroxy groups have on C_{tot} and highlight the shift of the potential of zero charge (PZC) relative to the pristine graphene surface, where the PZC is defined as the electrode potential where no excess charge is present on the metal electrode^[32,33]. This work provides additional insights compared to previous computational studies^[15,25]. Firstly, we do not report our results *vs.* the PZC, but *vs.* the standard hydrogen electrode (SHE), which allows a direct comparison between the different chemical systems. Secondly, we discuss the validity of the FBA performed in vacuum *vs.* different electrolytes using an implicit solvent model. We also report on the configurational probability distribution of nitrogen and boron substitutional doping and magnetism. We feel these additional insights will be beneficial to the research field.

2 Methods

We first employed the Vienna Ab-initio Simulation Package (VASP)^[34,35] to perform density functional theory (DFT) geometry optimizations to assess the energies of the optimized structures in vacuum. We used a $6 \times 6 \times 1$ supercell of graphene (72 atoms) in the hexagonal setting with space group $P6/mmm$ (191) as the starting point for our substitutional doping of carbon with boron and nitrogen. To explore the configurational space we utilized the Site-Occupancy Disorder (SOD) program, this allows the occurrence of a specific configuration to be described based on its energy and degeneracy giving a Boltzmann-like probability^[36]. We employed the generalized gradient approximation with the Perdew-Burke-Ernzerhof (PBE) exchange-correlation functional^[37]. A kinetic cutoff of 520 eV was used for the planewave expansion with a Γ -centered $4 \times 4 \times 1$ k -mesh for geometry optimizations with van der Waals molecular interactions included via the DFT-D3 method of Grimme with Becke-Jonson damping^[38,39]. Geometry optimizations were performed until the forces

between atoms were negligible (less than 0.01 eV/Å). This gave an optimized lattice parameter of 2.467 Å compared to the experimental value of 2.464 Å^[40], where we have used a vacuum spacing of 15 Å perpendicular to the graphene surface. Single point calculations were performed with a $6 \times 6 \times 1$ k -mesh and increased to $12 \times 12 \times 1$ where spin polarization was considered. The defect formation energy of each structural defect was determined using a larger $10 \times 10 \times 1$ supercell from

$$E_{\text{formation}} = E_{\text{defect}} - n\mu \quad (4)$$

where E_{defect} is the energy of the defective system, n is the number of carbon atoms and μ is the chemical potential, calculated from the total energy per carbon atom in pristine graphene. To model adsorbed oxygen and hydroxyl species optimizations were again performed in vacuum with the same convergence criteria and limited to one adsorption per unit cell to limit the complexity of the study.

For our electrochemical calculations, we employed the JDFTx code^[22], to model the graphene electrolyte interface, where we used a $6 \times 6 \times 1$ supercell for our substitutional systems and a larger $8 \times 8 \times 1$ supercell to account for the larger size of the structural defects. Geometries were re-optimized as a function of potential and converged when total energy differences were less 10^{-5} hartree. To eliminate the interaction between periodic images we used a vacuum spacing of 15 Å perpendicular to the graphene surface with a truncated Coulomb potential^[41]. Consistent with our VASP calculations we used the PBE functional with D3 van der Waals corrections^[37,42]. An ultrasoft pseudopotential was used to describe the core electrons^[43] and 20 hartree was used for the electronic plane-wave expansion. Electronic structure convergence was set to less than 10^{-8} hartree with a Fermi smearing of 0.005 hartree. Similar to the DFT calculations performed in vacuum single point calculations were performed on a Γ -centered $6 \times 6 \times 1$ k -mesh and increased to a $20 \times 20 \times 1$ Γ -centered k -mesh for the presentation of the DOS. For pristine graphene a $36 \times 36 \times 1$ Γ -centered k -mesh was used. The propylene carbonate (PC) solvent was modelled implicitly using the linear polarizable continuum model (LPCM)^[44], incorporating 1 mol/L concentration of NaCl anions and cations at 298 K. The absolute electrode potential of the surface was determined by taking the electronic chemical potential of the surface and then dividing by the elementary charge (-1), where the electronic chemical potential of the neutral surface is the PZC. We reference our theoretical results to the the experimental value of the SHE, 4.44 V. In comparison, the calibrated theoretical value for the LPCM solvation model in JDFTx was derived for noble metal surfaces in aqueous electrolyte and is of 4.68 V^[45]. In the low

doping regime, we find the graphene surfaces to be non-magnetic, and therefore non-spin polarized calculations for our implicit solvent models were used. As the JDFTx code only calculates the total capacitance, we separated the value into its constituent parts (C_Q and C_{EDL}) following the method of Zhan and Jiang^[15] that is based on the individual potential drops of C_Q and C_{EDL} across the interface. C_Q corresponds to the change in the number of electronic density of states (and thus the surface charge) as a function of the change in potential. Whereas C_{EDL} is the electrolyte response to charging and manifests itself through a shift of the density of states with a change in potential, with C_Q and C_{EDL} related to C_{tot} through Eq. (1). The total integrated capacitance was determined from the differential capacitance integrated over the studied potential range (−1 to 1 V) and expressed per unit of applied potential range^[46].

$$C_{tot}^{int} = \frac{1}{V} \int_0^V C dv \quad (5)$$

3 Results and discussion

3.1 Structural defects

Defects are ubiquitous to all real materials, with the type of defect and its corresponding defect density governed by its defect formation energy. In graphene, various structural point defects have been reported in the literature^[31,47]. Notably lattice reconstructions, where a C–C bond is rotated by 90° to form non-hexagonal rings, known as a Stone-Wales (SW) defect, as well as single vacancy (SV) and double vacancy (DV) defects^[48]. We have assessed the defect formation energies of 5 commonly reported structural defects (Figs. 2 and 3) in vacuum using a 10 × 10 supercell, with the pristine structure containing 200 atoms (Table 1). The number following the defect type indicates the defective ring (*i.e.* 5 for pentagon, 7 for heptagon and 8 for octagon). Our results are comparable to literature reported values, except for the SV defect which is found to be significantly lower^[31,49,50]. This may be due to the inclusion of magnetization in the DFT calculation leading to a reconstructed geometry. We find the magnetic configuration for the SV defect to be 0.33 eV lower in energy than the nonmagnetic configuration (Fig. 3). Furthermore, in the nonmagnetic configuration all the bond lengths are equal to 1.42 Å, whereas in the magnetic configuration there is significant deviation from a hexagonal arrangement with the formation of a five and nine-membered ring. This is consistent with the experiments of Ugeda et al.^[51] and DFT calculations reported by Banhart et al.^[31] and is explained by the weak covalent interaction between the two atoms

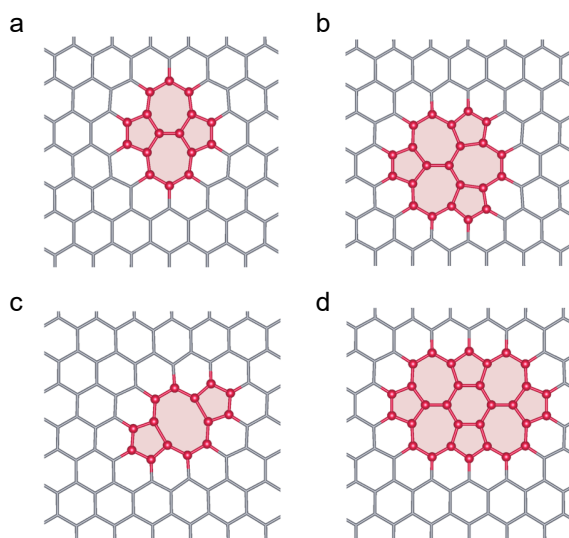


Figure 2 (a) Stone-Wales defect, (b) double vacancy (DV) 555-777 defect, (c) DV5-8-5 defect and (d) DV5555-6-7777 defect. Figure drawn using VESTA^[55].

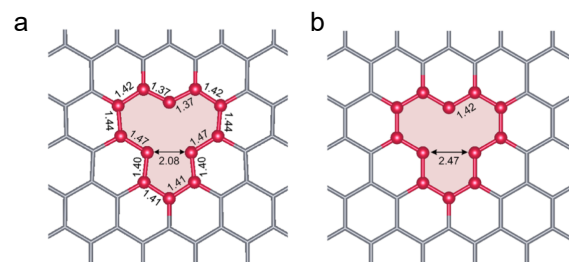


Figure 3 DFT optimized geometry of a single vacancy calculated in a 10 × 10 supercell in a magnetic configuration (a) and a nonmagnetic configuration (b). The magnetic configuration is found to be 0.33 eV lower in energy. In the nonmagnetic configuration all bond lengths are found to be 1.42 Å. Figure drawn using VESTA^[55].

Table 1 Graphene defect energies calculated in vacuum using a 10 × 10 supercell.

Defect type	Formation energy/eV		
	This work	Ref. [49]	Ref. [50]
Pristine	0.00	0.00	0.00
SW	4.70	5.29	4.9
DV555-777	6.52	6.34	6.6
DV5555-6-7777	6.81	7.34	6.9
SV	7.20	7.87	7.7
DV5-8-5	7.30	7.60	7.4

Note: Calculated defect formation energies are compared to Zhang et al.^[49] calculated using a 6 × 6 supercell and Rowe et al.^[50] calculated using a 10 × 10 supercell.

surrounding the vacancy^[48]. Indeed, this is further supported by our DFT results where we find a separation distance of 2.08 Å between the adjacent carbon atoms, rather than 2.42 Å in the nonmagnetic case. This difference in energy and geometry highlights the importance of including magnetization when studying SV defects, which is often ignored in computa-

tional studies. However, it is acknowledged that the SV defect is known to be extremely reactive and not present at room temperature^[52–54]. Therefore, to avoid computationally costly spin polarized calculations we have excluded the SV defect from our capacitance calculations.

The calculated defect formation energies are inherently large, indicating they are not thermodynamically favourable. However, the fabrication of graphene three-dimensional (3D) frameworks like graphene mesosponges (GMS)^[13] requires high synthesis temperatures (1173–2073 K). Moreover, the formation of these 3D frameworks occurs from the coalescence of graphene edge-sites on neighbouring domains through zipping reactions^[56] leading to the presence of polygons aside from pristine sp² hexagonal rings^[57–60].

The introduction of structural defects into graphene alters the electronic DOS and leads to a shift in the Fermi level. To determine these shifts, we use a $6 \times 6 \times 1$ supercell with 72 atoms for our dopants and a slightly larger $8 \times 8 \times 1$ supercell with 128 atoms for our topological defects due to the size of the defect. While the use of an $8 \times 8 \times 1$ supercell may lead to much higher defect densities compared to conventional carbon materials, highly porous carbons consisting of single-layer graphene walls and synthesized by a template method have been known to have a significantly higher number of defects^[56,59]. In this work we have chosen to use PC as an archetypal organic solvent, which has shown to exhibit good electrochemical stability, conductivity and performance and has been used in numerous experimental studies as well as commercial products^[29,61–63]. Our calculated DOS for graphene (Fig. S1) is in good agreement with the literature (calculated in vacuum)^[64], and with implicit solvent models using the PBE functional^[14,15,65]. In comparison, the DOS of graphene calculated at a higher level of theory using the Heyd-Scuseria-Ernzerhof (HSE) hybrid functional shows the same electronic structure around the Fermi level as the PBE functional. The difference between the two methods is that π and σ states are reported to extend to lower energy levels with the HSE functional (deviations appear at ~ 3 eV lower than the Fermi energy). Furthermore, there is very little difference reported in the position of the Fermi energy (~ 0.09 eV) between the HSE and PBE methods^[66]. As we consider a smaller energy range around the Fermi level (~ 1 eV) we use the PBE functional, and have added van der Waals corrections through the D3 method of Grimme^[38,39], leading to better agreement of calculated cell parameters (2.467 Å) with experiment 2.464 Å^[40], compared to 2.470 Å for PBE. Whilst the DOS for our structural defects (Fig. S1) is also in general agreement with the literature^[64], we have compared our DOS for each defect on an

absolute energy scale rather than aligning the Fermi energy of each structure to zero and present the DOS over a much smaller energy scale. We align the energy levels to that of the SHE at -4.44 eV^[67], this allows a direct comparison between each system and is useful for our later discussion. For each structural defect electronic states are found to be removed from the system and the Fermi level is shifted downward in energy (Fig. S1). Hence, the introduction of structural defects leads to *p*-type doping, with the largest Fermi shift occurring with the introduction of two carbon vacancies (DV systems). The smallest (almost negligible) Fermi level shift and smallest change in the DOS is observed for the SW defect, this is not surprising as a SW defect does not contain any vacancy. A SW defect also has the lowest formation energy and therefore may be the most predominant defect. Although, it has been reported that a SW defect may heal itself through the rotation of the two defective carbon atoms to their original position (a process requiring a substantial ~ 4.4 eV of energy is unlikely to be overcome at an annealing temperature of 2073 K)^[68]. Furthermore, zipping reactions are unlikely to be stoichiometric, so a number of DV555-777 defects, may also be present. We suggest the other higher energy defects (SV, DV5-8-5, DV5555-6-7777) that have also been observed experimentally using electron irradiation^[69], are unlikely to be present in any significant quantity due to their significantly larger defect formation energies. From the DOS we see that a DV555-777 defect introduces the largest number of electronic states at lower energy levels, whereas DV5-8-5 defects introduces empty states in the conduction band. The increase in the number of states ultimately leads to a higher C_Q and will be discussed later. In contrast, the introduction of a SW defect leads to the smallest change in the overall DOS and would be expected to have the smallest change C_Q .

3.2 Substitutional doping

Structural defects introduced into graphene remove electronic density of states, leading to *p*-doped graphene. To realize an *n*-doped system, an excess of electronic states must be introduced. This can be achieved with the substitution of carbon atoms for nitrogen (nitrogen has one additional electron) to form graphitic nitrogen. The opposite effect would occur with the substitution of a carbon atom for boron, as an electron is removed. This study focuses on graphitic substitutional defects over pyrrolic and pyridinic N as these have been shown to be most stable defect, especially at annealing temperatures greater than 1000 °C, above which, thermal decomposition occurs^[18]. Moreover, the doping concentration is kept below 5% consistent with the N concentration found incorporated into GMS from previous

work^[18]. To investigate the effect of substitutional doping on the electronic structure, we first explore the configurational space of the doped systems. The substitution of one carbon atom with nitrogen (1.6 wt%) or boron atom (1.3 wt%) in a 72-atom supercell is trivial. The dopant atom can reside at any carbon position and all configurations are equivalent, hence the energy of only one configuration needs to be evaluated. At higher dopant concentrations the configurational space to be explored increases, leading to a larger number of configurations needing to be evaluated. Considering the symmetry of the lattice there are 15 inequivalent configurations out of 2,556 possible configurations for two carbon substitutions (Fig. S2) or 167 inequivalent configurations (out of a total of 59,640 configurations) for three substitutions (~4.8 wt% nitrogen or ~3.8 wt% boron). By evaluating the probability distribution of the different configurations of nitrogen (N)- and boron (B)-doped graphene for two atomic substitutions (~3.2 wt% nitrogen and ~2.5 wt% boron) we find that the most likely configurations are where the dopant atoms are segregated. For computational efficiency and in-line with the experimental results reported by Błoński et al.^[70], we performed the full configurational analysis in vacuum using VASP. Test calculations using JDFT yield a similar configurational-energy relationship and we report the energy of each configuration in Table S1. In Fig. 4 we present the configurational probability distribution of the three most likely configurations (1–3), which are all found to be non-

magnetic and two configurations (4 and 5) that exhibit magnetic ordering, evident from the asymmetry in the up and down spin channels of their respective DOS (Fig. S3). Taking the difference between the number of electrons in each channel yields, a magnetization of 0.34 and 0.52 μ_B per supercell for configuration 4 and 5 respectively in the N-doped system and 0.05 and 0.50 μ_B for the B-doped system. Configuration 1 is found to have the lowest energy at 0 K (Table S1) and is therefore the most stable configuration. This indicates preferential segregation of the dopant atoms, in contrast the highest energy (least stable structure) is found to be where boron or nitrogen atoms are adjacent to each other at about 1.2 eV higher in energy. Moreover, at the chemical vapor deposition synthesis temperatures of 1073 K used in the work of Błoński et al.^[70] and the synthesis temperature of 1173 K used by Nishihara et al.^[13], our theoretical results indicate the most favored configuration is nonmagnetic (Fig. 4). This observation elucidates the reason for the observed ferromagnetism in N-doped graphene for concentrations of greater than 5 at%, where synthesis was performed using a combination of exfoliation and reduction of graphite oxide at temperatures of up to 1073 K^[70]. At low doping concentrations, nitrogen is segregated throughout the graphene basal plane and nitrogen centers are too far apart to induce magnetic ordering. The DOS of our doped systems (Figs. S4 and S5) also shows that the Fermi level is shifted in energy but there are no significant changes in the electronic structure around

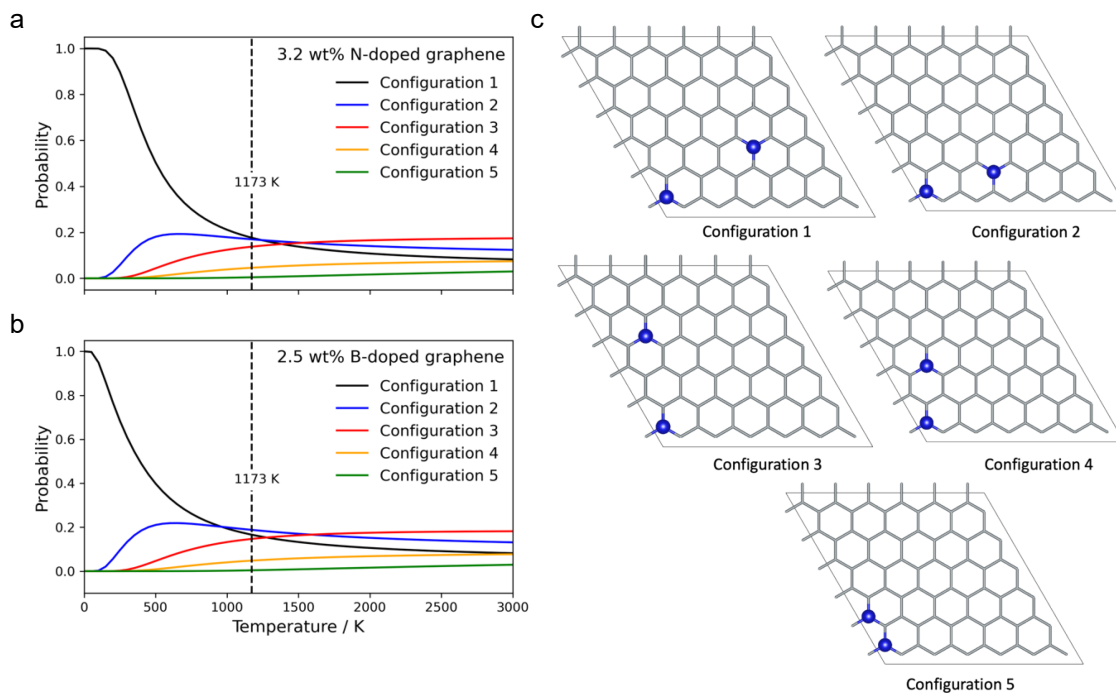


Figure 4 Probability distribution of 5 selected configurations for 3.2 wt% N-doped graphene (a) and 2.5 wt% B-doped graphene (b). The dashed line indicates the chemical vapor deposition temperature of 1173 K^[13]. (c) Corresponding configurations drawn using VESTA^[55], configurations 1, 2 and 3 are found to be non-magnetic, whereas configurations 4 and 5 are found to be magnetic (carbon = grey, nitrogen or boron = blue).

the Fermi level of graphene (in contrast to the large changes in the DOS observed for the structural defects. This suggests nitrogen or boron doping would lead to a lower change in C_Q compared to the introduction of structural defects around the Dirac point. Lastly, we report that in our pyridinic nitrogen model, where we substitute 3 neighboring carbon atoms with nitrogen and introduce a carbon vacancy (Fig. S6), a *p*-type doped system is realized, with the Fermi level shifted to a lower energy level. The atomic origin of this *p*-type character can be attributed to the electron count. The 3 additional electrons introduced by substitution of carbon atoms with nitrogen are overcompensated by a carbon vacancy, leading to a net loss of one electron and a shift of the Fermi level into the valence band.

3.3 Functionalized graphene oxide

Graphene oxide containing hydroxy, epoxy and carboxy groups is easily produced at large scale and often a precursor to many graphene based materials^[71]. As a material for supercapacitors, reduced graphene oxide with a number of these groups removed is preferable due to its increased conductivity^[72]. As hydroxy and epoxy groups are more likely to be present on the basal plane of graphene, in comparison to carboxy groups that form at edge sites, and are removed through zipping reactions^[73], we focus on the properties of epoxy and hydroxy functionalized graphene (Fig. S7) with one surface oxygen corresponding to 1.8 wt% oxygen, with their corresponding DOS shown in Fig. S8. The presence of such groups leads to an sp^2 -to- sp^3 transition on the bonded carbon and a shift in the Fermi level to lower energy levels that is more pronounced for hydroxy than epoxy groups. For 1.6 wt% N-doped graphene additional configurational disorder is introduced due to the number of possibilities of where oxygen can bind. Exploring the configurational space, we find the lowest energy (most probable) configuration is where oxygen is bonded to the carbon atom adjacent to the nitrogen, forming an amide-type functional group (Fig. S7). This configuration is more stable by ~ 0.2 eV compared to the where oxygen is bonded to the next nearest carbon atom. Furthermore, the Fermi energy is shifted down in energy by 0.46 eV compared to pristine graphene. The *n*-type nitrogen system is counteracted by the presence of oxygen leading to a *p*-type system. This effect is also highly dependent on the configurational space and the oxygen binding site. Where oxygen is bound to the next nearest neighbor carbon atom the effect is somewhat less pronounced and the system remains slightly *n*-type with the Fermi energy higher by ~ 0.06 eV compared to pristine graphene. These results indicate that by carefully selecting the dopants and their respective concentrations one can carefully

tune the Fermi level (and the PZC) to the desired potential.

3.4 Potential of zero charge

In Fig. 5 we show the calculated PZC for our studied systems. Here following JDFT the potential of the bulk electrolyte is taken as zero^[44]. We take the absolute potential of the SHE to be the experimentally estimated value of 4.44 V. This gives better alignment of our results over the theoretical LPCM value of 4.68 V, which was calibrated in JDFT on noble metals surface in aqueous electrolyte. The PZC of pristine graphene corresponds to its minimum capacitance, dictated by its Dirac point, and the limited number of electronic states around the Fermi level^[74]. A quantitative comparison to experimentally reported values indicate our calculated PZC for pristine graphene in PC of -0.56 V *vs.* the SHE is underestimated by ~ 0.35 V. Xia et al. report a value of -0.2 V *vs.* the SHE (measured in an ionic liquid)^[16]. A more comparable experimental value using a similar PC electrolyte is reported by Tang et al., that is about -0.25 V *vs.* the Ag/AgClO₄ electrode^[29]. Converting this value to the SHE scale using the relation $E_{\text{SHE}} = E_{\text{Ag/AgClO}_4} + 0.66$ V^[75], we find an underestimation of ~ 0.35 V. This deviation is comparable to other studies in different electrolytes using the PBE functional. For example, the computational study by Zhan and Jiang using JDFT and an implicit model of 6 mol/L KOH aqueous electrolyte reported the Fermi level to be -0.15 a.u. This also corresponds to the Dirac point at about -0.35 V *vs.* the SHE compared to experimentally reported results of ~ 0 V *vs.* the SHE using the same electrolyte^[8]. Whilst the theoretical PZC is highly dependent on the DFT functional and implicit solvent model, our theoretical model also corresponds to the potential of zero free charge with no adsorption of ions from the electrolyte and a pristine surface free of intrinsic defects, which also affects the electronic structure and PZC. This may introduce an additional discrepancy compared to experimental values that is also observed for the PZC calculated for Cu surfaces^[44]. In vacuum, Puschnig and Lüftner report a work function energy of 4.28 eV compared to our results of 4.26 eV, indicating an underestimation of ~ 0.18 eV for graphene using the PBE functional when referenced to the SHE^[66]. These errors are close to the expected deviation of ~ 0.3 eV for the PBE functional and much smaller than that of the local density approximation, suggesting part of the discrepancy can be attributed to the PBE functional^[76], and part due to the limitations of the LPCM. A similar discrepancy has been reported in determining the work function of Pt(111)/water interfaces using the ONETEP DFT code and partly attributed to the PBE functional, and partly to the orientational dipole moment of the water molecules

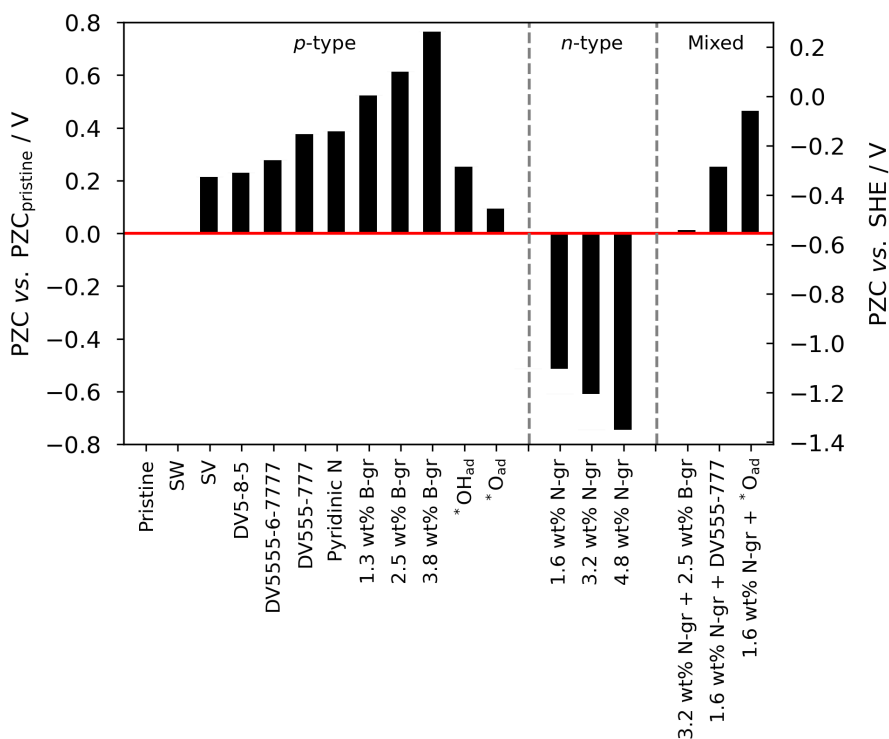


Figure 5 Calculated PZC of the structural defects and adsorbed functionalized groups onto a graphene surface. Referenced against the both the PZC of pristine graphene and the SHE.

at the surface with further parametrization or the use of the rVV10 functional proposed as a remedy^[77]. An additional remedy maybe the inclusion of a surface layer of solvent molecules in a hybrid explicit/implicit approach, but this has not been considered due to the computational complexity in dealing with the orientation of the solvent molecules that typically requires a statistical ensemble approach. Focusing on the variation of the PZC from Fig. 5, we see a clear shift in the PZC to different potentials for the different studied systems, this would not be apparent if the PZC of each system was referenced to zero. The incorporation of structural defects, pyridinic groups, B-doping, and surface epoxy or hydroxy groups act as *p*-type dopants shifting the PZC to higher potentials (lower Fermi energies). In contrast, substitutional N-doping, acts as a *n*-type dopant shifting the PZC to lower potentials. Interestingly, we find that if mix *p*- and *n*-type dopants, we can recover the PZC of pristine graphene. For example, when co-doping graphene with 2 atoms of nitrogen and 2 atoms of boron, they counteract each other and the PZC reverts to that of pristine graphene (to within 6 meV). In this mixed system the curvature of the DOS around the Fermi level (Fig. S5) is found to retain the minimum around the Dirac point suggesting a large change in capacitance would not be achieved. In the case of one nitrogen substitution with a structural (DV555-777) defect, we find a somewhat additive effect with the

resultant system being *p*-type, however, a full configurational analysis was not performed. On co-doping with oxygen and graphitic nitrogen the scenario is more complicated, we find preferential binding of oxygen to the carbon adjacent to the nitrogen forming an amide-type group leading to a *p*-type doped system. Hence, careful doping emerges as a tool to fine tune the PZC to a selected area of the DOS. However, to increase C_{tot} we need to increase C_{Q} by either moving further away from the PZC of pristine graphene or by introducing defects to increase the number of electronic states around the graphene's Dirac point.

3.5 Capacitance

Consistent with our values for the PZC in Fig. 5, we present our capacitance data referenced against the SHE (Fig. 6), calculated by taking the derivative of the surface charge against potential (Fig. S9). In our analysis, we integrate C_{tot} over the presented potential range (-1.0 to 1.0 V vs. pristine graphene) and also report $C_{\text{tot}}^{\text{int}}$. The minimum capacitance (C_{min}) is clearly visible for pristine graphene at the PZC and is shifted to higher and lower potentials with the increasing the number of graphitic substitutions. This is consistent with experimental work on N-doped graphene and our previous work on N-doped zeolite-templated carbon^[9,63]. Substitutional doping at low concentrations does not lead to a comparatively large change in the C_{tot} , only a shift of the PZC,

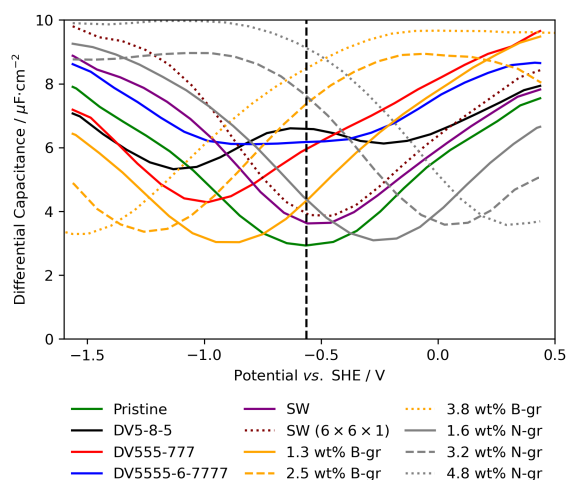


Figure 6 Total differential capacitance referenced against the SHE. Calculated with a $8 \times 8 \times 1$ supercell for the structural defects and a $6 \times 6 \times 1$ supercell for the N- and B-doped systems. The dotted purple line indicates the differential capacitance of a SW defect calculated using a smaller $6 \times 6 \times 1$ unit-cell.

which is directly related to the shift in the Fermi energy (Figs. S4 and S5). Hence, substitutional defects do not lead to a significant increase in the capacitance around graphene's Dirac point. In comparison structural defects lead to more significant changes in the electronic structure and a larger increase in C_{tot} . For the case of a SW defect, there is a small shift in the PZC and a larger C_{tot} , consistent with more available electronic states in the DOS (Fig. S1). For comparison, we also include an SW defect calculated in a smaller $6 \times 6 \times 1$ supercell to compare to the $8 \times 8 \times 1$ supercell. As can be seen in Fig. 6 there is a small upshift in the capacitance curve due to the increase in defect density. Compared to pristine graphene the increase in the minimum capacitance is also observed for the other structural defects. The largest change in C_{tot} is found for DV5555-6-7777 and DV555-777 defects. For DV555-777, as we move to lower energies compared to the Fermi energy of pristine graphene the number of available DOS increases and the differential capacitance increases at higher potentials (Fig. 6). Large changes in the capacitance curves are inconsistent with the butterfly shape curves generally reported for pristine graphene and 3D graphene frameworks^[29], suggesting they do not form in any significant quantity. This is supported by their larger calculated defect formation energies reported in Table 1. Although, one route to artificially introducing more structural defects may be able through electron irradiation^[69]. Furthermore, the recently synthesized monolayer amorphous carbon synthesized by laser-assisted chemical vapor deposition exhibits a large distribution of non-hexagonal membered rings with a large density of states around the Fermi level and clear metallic character, indicating its potential for

supercapacitor applications^[78]. It is worth noting that on charging to a specific potential the number of introduced electronic states is not fully realized because of an additional shift in potential of the DOS (Fig. S10). This leads to the Dirac point shifting in position, limiting the number of additional states incorporated on charging, and is due to the electrolyte response (C_{EDL}).

As C_{EDL} is found to be relatively constant^[8], the observed curvature in the differential capacitance is expected to be largely dictated by C_{Q} . This suggests it may be justified to only consider the DOS in determining C_{Q} following the FBA. To address this, we analyzed the DOS of the neutral and positively charged pristine graphene (Fig. S10). When we charge the surface by 1 eV, we find the shape of the DOS to be similar, but we see a band shift to lower energy levels, leading to a smaller change in the DOS than if no band shift occurred. This band shift is the response of the electrolyte to the surface charge and gives rise to C_{EDL} , whereas band filling gives rise to C_{Q} . We use this method^[15] to separate the C_{tot} into its constituent (C_{EDL} and C_{Q}) components (Fig. S11), with the results of the integrated capacitance shown in Table S2. Firstly, as the PZC is directly related to the Fermi level and is shifted depending on the dopant or defect, unlike pristine graphene the PZC does not align with the minimum C_{Q} (Fig. 7). Secondly, substitutional doping with N or B is much more effective at moving the PZC away from C_{min} but does not greatly affect the curvature of the capacitance curve (a similar effect is seen for adatom doping, and is discussed below). In contrast, structural defects realize a small change in the PZC but introduce slightly more DOS around the Dirac point leading to a slightly larger capacitance. This is clearly evident for DV5-8-5 and DV5555-6-7777 (Figs. 7b and 7d). Thirdly, the curvature of C_{Q} follows C_{tot} with C_{EDL} remaining relatively constant at $\sim 18 \mu\text{F cm}^{-2}$, where in our model we have used PC as the solvent with a dielectric constant of 64^[79]. The deviation from linearity for C_{EDL} is largely attributed to manually resolving the small changes in the shift of density of states in order to separate C_{tot} into its individual contributions. The calculated C_{EDL} of $\sim 18 \mu\text{F cm}^{-2}$ is slightly lower than the value reported by Zhan et al. ($\sim 21 \mu\text{F cm}^{-2}$) and may be ascribed to the lower dielectric constant of PC used in this study compared to that of the aqueous electrolyte used in their work (78.4)^[65]. In comparison an experimental study using PC by Tang et al. report a C_{EDL} of $\sim 10 \mu\text{F cm}^{-2}$ ^[29] suggesting our value may be overestimated and possibly a limitation of the LPCM. Current approaches to modelling C_{EDL} typically involve molecular dynamics calculations^[46] or taking C_{EDL} from experiment^[80] and combining these results electronic structure calculations to determine C_{Q} using

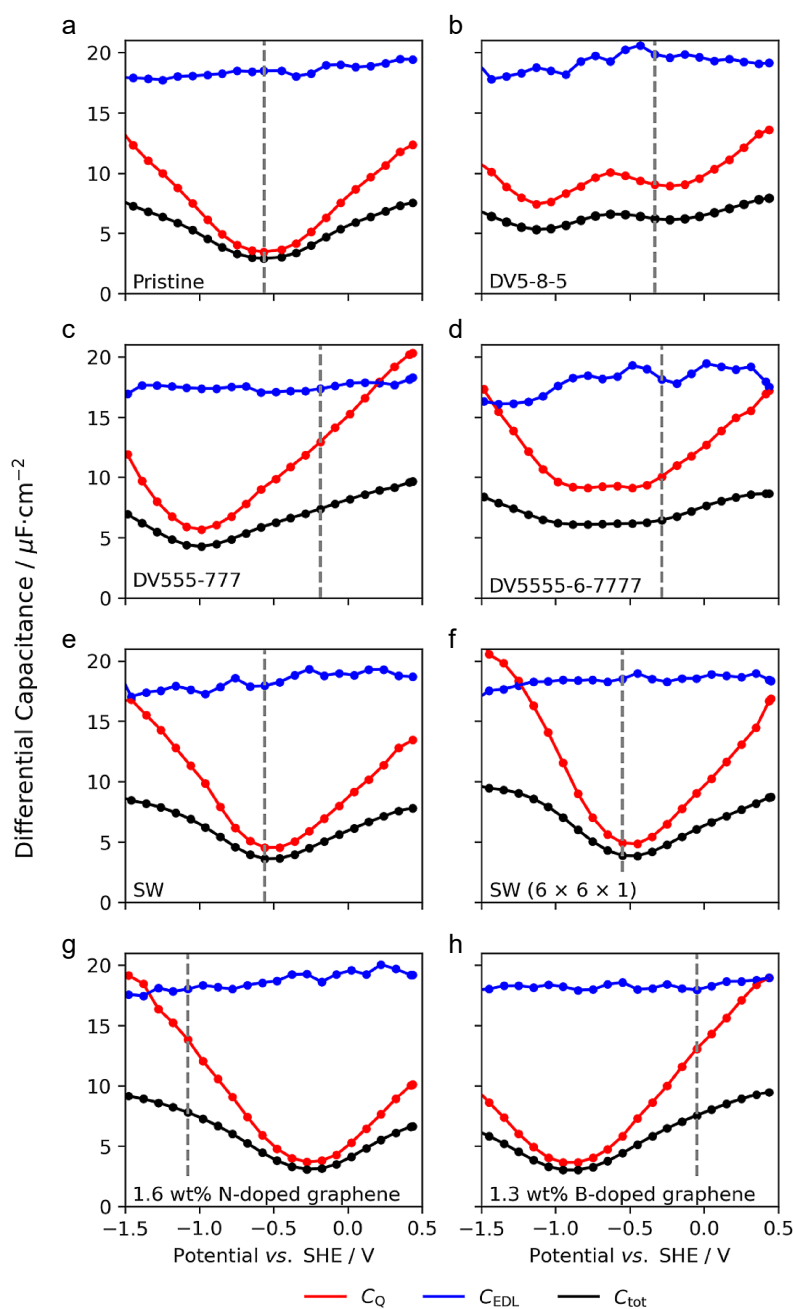


Figure 7 Total differential capacitance separated into C_Q and C_{EDL} , and referenced against the SHE for the studied structural defects (a–f), 1.6 wt% N-doped graphene (g), and 1.3 wt% B-doped graphene (h). The vertical dashed vertical lines indicate the calculated PZC for each system.

the FBA. This approach neglects the interaction between the solvent and the charged surface. In JDFT this interaction is accounted for through the band shift of the DOS. At greater computational cost these interactions could be more accurately investigated using AIMD^[77], which for aqueous water electrolyte has been reported with good agreement to experiment^[81]. However, to the authors' knowledge, no similar AIMD study has been reported using a PC electrolyte. This band shift is dependent on the solvent (dielectric constant) used in the implicit solvent model and for pristine graphene when charg-

ing the surface to 1 V we observe a band shift of ~ 0.35 V (and hence band filling occurs over 0.65 V). If the dielectric constant is reduced this band shift increases leading to a reduction of C_{EDL} . To illustrate this, we change the solvent to dimethyl carbonate with a dielectric constant of 3.1. On charging to 1 V C_{EDL} the band shift is 0.50 V, leading to a decrease in C_{EDL} to 8 $\mu\text{F}\cdot\text{cm}^{-2}$. The effect of the electrolyte (implicit solvent) cannot be ignored as it leads to band filling occurring over a smaller potential range, and this is more prevalent for solvents with lower dielectric constants. We conclude that while the FBA

correctly reproduces the DOS over small potential ranges on charging and discharging^[82], it does not shift the DOS in energy, leading to erroneous results, and is also unable to determine C_{EDL} . Hence, to justify the use of the computationally efficient FBA (over a small potential range), one approach we propose is to determine the band shift theoretically or use experimentally determined values for a given solvent, and then perform FBA calculations shifting the DOS accordingly to account for the electrolyte response on charging. In Fig. S12 we show the capacitance curves for pristine graphene, pyridinic nitrogen (Fig. S6a), and the epoxy and hydroxy systems. As in the case of our structural defects, C_{EDL} remains relatively constant, again with the error attributed to the manual separation of C_Q and C_{EDL} . From the DOS we find C_Q increases away from C_{min} , which is dictated by the Dirac point of graphene. Theoretically the minimum C_Q should approach close to zero at graphene's Dirac point and have a linear gradient around the PZC, whereas we calculate a value of $3.4 \mu\text{F cm}^{-2}$ with a parabolic curvature around the PZC. The discrepancy is due to the electronic smearing parameter used in these calculations, where we use an electronic smearing parameter of 0.005 hartree (Fig. S13). This leads to more rapid convergence, and gives results more in line with experimental values for pristine graphene, which contain defects and charge carriers^[16,29]. Furthermore, reducing the smearing parameter to 0.001 hartree doesn't lead to a change in the calculated Fermi level. The largest change in C_Q is seen with $*\text{O}_{ad}$ shifting the minimum C_Q from $3.4 \mu\text{F cm}^{-2}$ to $4.1 \mu\text{F cm}^{-2}$ (compared to a minimum of $9.1 \mu\text{F cm}^{-2}$ found for DV555-777). An experimental study by Hassan et al. report a minimum C_Q of $3.8 \mu\text{F cm}^{-2}$ for pristine graphene increasing to a maximum of $11.1 \mu\text{F cm}^{-2}$ after oxidation for 400 s, with an evident loss of curvature in the capacitance curves with their results also indicating a small potential shift of C_Q minimum as a function of oxidation time^[83].

As the total charge capacity is based on the integrated capacitance over a charge–discharge cycle, the integrated capacitance (C_{tot}^{int}) can be expressed as the total charge storage capacity per unit of applied potential.

The largest increase for the DV defects is for DV5555-6-7777 with C_{tot}^{int} increasing from 5.2 to $7.1 \mu\text{F cm}^{-2}$ over the potential range (-1 to $+1$ V vs. PZC of pristine graphene; Table S2). For pyridinic nitrogen, C_{min} is shifted downwards in potential (the opposite trend to graphitic nitrogen) and a maximum capacitance observed at around 0.1 V vs. the SHE (Fig. S12b). In contrast to the work of Ochoa-Calle we do not observe a large peak in the total capacitance near the PZC, rather C_Q is still increasing and its effect on C_{tot} is less pronounced. This may

be due to modelling a different electrolyte or the smaller supercell used (4×4 vs. 6×6 in this work), leading to a larger structural change and dopant concentration (9.7 at% pyridinic nitrogen vs. 4.2 at% in this work) and a greater shift in the Fermi level^[25]. Overall, we find structural defects especially DV-defects lead to a larger introduction of density of states around the Dirac point, increasing the minimum C_Q in the butterfly shaped capacitance curve. Whereas the surface adsorbed species and the pyridinic structure tend to increase C_Q further away from the minimum, with substitutional defects having a large impact on the PZC but not significantly altering the capacitance.

The substantially larger capacitance for the DV defects around the Dirac point suggests increasing the number of structural defects (particularly DV defects) is the preferred mechanism to enhancing C_Q , while dopants could be utilized to tune the PZC to the desired potential. These results are in somewhat agreement with the work Chen et al. who show both structural defects and N-dopants can tune the Fermi level and increase C_Q ^[9]. However, in their study only a SW defect was considered, which we have found to have the least effect of the structural defects on C_Q and only a slightly larger effect than 1.6 wt% N-doped graphene. In contrast, we show the inclusion of DV defects, leads to significantly larger changes in the DOS and a larger realized C_Q . Furthermore, as the energy density (E) is dictated by both its capacitance and voltage ($E = 1/2CV^2$) it is also necessary to mention the effect of V . In previous work we have shown that carbon edge sites and oxygen-functional groups cause a low voltage stability^[84]. Moreover, we demonstrated that edge-site free GMS with basal defects can achieve the highest voltage stability among high-surface carbon materials^[73]. Therefore, SV defects and the oxygen-functional groups shown in this work are not preferable to achieve high V . The most promising structure to achieve high energy density would be basal defects, specifically DV5555-6-7777, rather than heteroatom doping. This is an important conclusion as GMS is expected to achieve such a target from its edge-free and basal-defect-rich properties. However, GMS still shows a low C_Q ^[29], suggesting that low energy defects such as SW dominate in GMS, thus having a limited effect on the C_Q . Therefore, we suggest that if the number of effective basal defects like DV5555-6-7777 can be incorporated into the structure, the material would show great promise for future high-energy-density supercapacitors.

4 Conclusion

We have investigated how structural carbon defects, nitrogen- and boron-doping, and the addition of

adatoms affect the electronic structure of graphene, and determined their corresponding capacitance using JDFT. We highlight the difference in the optimized geometries of the SV defect based on the inclusion of spin polarisation in our DFT calculations. The lowest energy configurations for nitrogen and boron substitutions in graphene exhibit a segregation of their dopant atoms. We rationalize this segregation is the reason behind the magnetic transition for N-doped graphene only being experimentally observed at higher doping levels. The large defect formation energies for the DV vacancies and the flatter curvature in their capacitance curves suggest they are unlikely to be present in any significant density. We confirm that while the fixed band approximation (over a small potential range) exhibits a similar DOS in both the charged and neutral systems, the shift of the DOS, which is related to C_{EDL} is dependent on the electrolyte. Hence, the FBA is not valid in determining the capacitance, unless the effect of the electrolyte and the resultant band shift are also considered. Our results suggest the incorporation of more structural defects in graphene (particularly DV defects), rather than substitutional doping with boron or nitrogen, or adatom doping with epoxy or hydroxy groups leads to the largest increase in capacitance around the Dirac point of graphene. However, substitutional and the addition of adatoms leads to a greater shift of the PZC away from the Dirac point. We anticipate this study will provide a framework to guide experimentalists with doping strategies to optimize graphene-based materials for EDL applications and raises important considerations for theoreticians to perform computationally efficient and accurate results that can be aligned with experiment.

Acknowledgements

A.A. is grateful to the JSPS for his JSPS fellowship. D.D.T. and R.C.O. thank the UK's Royal Society International Exchange Programme (IEC\R3\193106).

Author contribution statement

A.A. and H.N directed the project, analyzed the results, and wrote the manuscript. A.A performed the theoretical calculations. R.T. and W.Y helped analyze the results providing useful experimental input. R.C.O and D.D.T. advised on the theory. All the authors discussed and analyzed the data, and approved the final manuscript.

Data availability

The data that support the findings of this study is

available from the corresponding author upon reasonable request.

Declaration of competing interest

All the contributing authors report no conflict of interests in this work.

Funding

This work was supported partially by JST SICORP (Grant No. JPMJSC2112) and JST Adaptable and Seamless Technology Transfer Program through Target-driven R&D (A-STEP) (Grant No. JPMJTR22T6), and JSPS KAKENHI (Grant No. 22K14757). Calculations were performed using the U.K. National Supercomputing Facility ARCHER2 (<http://www.archer2.ac.uk>) via our membership of the U.K.'s HEC Materials Chemistry Consortium, which is funded by the EPSRC (Grant Nos. EP/L000202 and EP/R029431) and the Molecular Modelling Hub for computational resources, MMM Hub, which is partially funded by EPSRC (Grant No. EP/P020194/1). This research has also utilized Queen Mary's Apocrita HPC facility, supported by QMUL Research-IT.

Use of AI statement

None.

Electronic Supplementary Material: Supplementary material is available in the online version of this article at <https://doi.org/10.26599/EMD.2024.9370035>

References

- [1] Blanco, H., Faaij, A. (2018). A review at the role of storage in energy systems with a focus on Power to Gas and long-term storage. *Renew. Sustain. Energy Rev.* 81, 1049–1086.
- [2] Zhang, L. L., Zhao, X. S. (2009). Carbon-based materials as supercapacitor electrodes. *Chem. Soc. Rev.* 38, 2520–2531.
- [3] Simon, P., Gogotsi, Y. (2008). Materials for electrochemical capacitors. *Nat. Mater.* 7, 845–854.
- [4] Sun, J. L., Luo, B. C., Li, H. X. (2022). A review on the conventional capacitors, supercapacitors, and emerging hybrid ion capacitors: past, present, and future. *Adv. Energy Sustain. Res.* 3, 2100191.
- [5] Pershaanaa, M., Bashir, S., Ramesh, S., Ramesh, K. (2022). Every bite of Supercap: a brief review on construction and enhancement of supercapacitor. *J. Energy Storage* 50, 104599.
- [6] Ke, Q. Q., Wang, J. (2016). Graphene-based materials for supercapacitor electrodes – A review. *J. Materiomics* 2, 37–54.
- [7] Tan, C. L., Huang, X., Zhang, H. (2013). Synthesis and applications of graphene-based noble metal nanostructures. *Mater. Today* 16, 29–36.

- [8] Ji, H. X., Zhao, X., Qiao, Z. H., Jung, J., Zhu, Y. W., Lu, Y. L., Zhang, L. L., MacDonald, A. H., Ruoff, R. S. (2014). Capacitance of carbon-based electrical double-layer capacitors. *Nat. Commun.* 5, 3317.
- [9] Chen, J. F., Han, Y. L., Kong, X. H., Deng, X. Z., Park, H. J., Guo, Y. L., Jin, S., Qi, Z. K., Lee, Z., Qiao, Z. H., et al. (2016). The origin of improved electrical double-layer capacitance by inclusion of topological defects and dopants in graphene for supercapacitors. *Angew. Chem. Int. Ed.* 55, 13822–13827.
- [10] Lv, S., Ma, L. Y., Shen, X. Y., Tong, H. (2021). Recent design and control of carbon materials for supercapacitors. *J. Mater. Sci.* 56, 1919–1942.
- [11] Saha, D., Li, Y. C., Bi, Z. H., Chen, J. H., Keum, J. K., Hensley, D. K., Grappe, H. A., Meyer III, H. M., Dai, S., Paranthaman, M. P., et al. (2014). Studies on supercapacitor electrode material from activated lignin-derived mesoporous carbon. *Langmuir* 30, 900–910.
- [12] Zhai, Y. P., Dou, Y. Q., Zhao, D. Y., Fulvio, P. F., Mayes, R. T., Dai, S. (2011). Carbon materials for chemical capacitive energy storage. *Adv. Mater.* 23, 4828–4850.
- [13] Nishihara, H., Simura, T., Kobayashi, S., Nomura, K., Berenguer, R., Ito, M., Uchimura, M., Iden, H., Arihara, K., Ohma, A., et al. (2016). Oxidation-resistant and elastic mesoporous carbon with single-layer graphene walls. *Adv. Funct. Mater.* 26, 6418–6427.
- [14] Radin, M. D., Ogitsu, T., Biener, J., Otani, M., Wood, B. C. (2015). Capacitive charge storage at an electrified interface investigated via direct first-principles simulations. *Phys. Rev. B* 91, 125415.
- [15] Zhan, C., Jiang, D. E. (2016). Contribution of dielectric screening to the total capacitance of few-layer graphene electrodes. *J. Phys. Chem. Lett.* 7, 789–794.
- [16] Xia, J. L., Chen, F., Li, J. H., Tao, N. J. (2009). Measurement of the quantum capacitance of graphene. *Nat. Nanotechnol.* 4, 505–509.
- [17] Wu, J. Z. (2022). Understanding the electric double-layer structure, capacitance, and charging dynamics. *Chem. Rev.* 122, 10821–10859.
- [18] Tang, R., Aziz, A., Yu, W., Pan, Z. Z., Nishikawa, G., Yoshii, T., Nomura, K., Taylor, E. E., Stadie, N. P., Inoue, K., et al. (2024). Prominent structural dependence of quantum capacitance unraveled by nitrogen-doped graphene mesosponge. *Small* 20, 2308066.
- [19] Shylau, A. A., Kłos, J. W., Zozoulenko, I. V. (2009). Capacitance of graphene nanoribbons. *Phys. Rev. B* 80, 205402.
- [20] Abidi, N., Lim, K. R. G., Seh, Z. W., Steinmann, S. N. (2021). Atomistic modeling of electrocatalysis: are we there yet?. *WIREs Comput. Mol. Sci.* 11, e1499.
- [21] Sundararaman, R., Vigil-Fowler, D., Schwarz, K. (2022). Improving the accuracy of atomistic simulations of the electrochemical interface. *Chem. Rev.* 122, 10651–10674.
- [22] Sundararaman, R., Goddard III, W. A., Arias, T. A. (2017). Grand canonical electronic density-functional theory: algorithms and applications to electrochemistry. *J. Chem. Phys.* 146, 114104.
- [23] Wood, B. C., Ogitsu, T., Otani, M., Biener, J. (2014). First-principles-inspired design strategies for graphene-based supercapacitor electrodes. *J. Phys. Chem. C* 118, 4–15.
- [24] Bandaru, P. R., Yamada, H., Narayanan, R., Hofer, M. (2017). The role of defects and dimensionality in influencing the charge, capacitance, and energy storage of graphene and 2D materials. *Nanotechnol. Rev.* 6, 421–433.
- [25] Ochoa-Calle, A., Guevara-Garcia, A., Vazquez-Arenas, J., González, I., Galván, M. (2020). Establishing the relationship between quantum capacitance and softness of N-doped graphene/electrolyte interfaces within the density functional theory grand canonical kohn-sham formalism. *J. Phys. Chem. A* 124, 573–581.
- [26] Cui, D. D., Li, H. J., Li, M. J., Li, C. P., Qian, L. R., Zhou, B. Z., Yang, B. H. (2019). Boron-doped graphene directly grown on boron-doped diamond for high-voltage aqueous supercapacitors. *ACS Appl. Energy Mater.* 2, 1526–1536.
- [27] Zhan, C., Zhang, P. F., Dai, S., Jiang, D. E. (2016). Boron supercapacitors. *ACS Energy Lett.* 1, 1241–1246.
- [28] Xu, Q., Yang, G. M., Fan, X. F., Zheng, W. T. (2019). Improving the quantum capacitance of graphene-based supercapacitors by the doping and co-doping: first-principles calculations. *ACS Omega* 4, 13209–13217.
- [29] Tang, R., Nomura, K., Inoue, K., Kotani, M., Kyotani, T., Nishihara, H. (2022). Capacitance of edge-free three-dimensional graphene: new perspectives on the design of carbon structures for supercapacitor applications. *Electrochim. Acta* 429, 141009.
- [30] Sunahiro, S., Nomura, K., Goto, S., Kanamaru, K., Tang, R., Yamamoto, M., Yoshii, T., Kondo, J. N., Zhao, Q., Nabi, A. G., et al. (2021). Synthesis of graphene mesosponge via catalytic methane decomposition on magnesium oxide. *J. Mater. Chem. A* 9, 14296–14308.
- [31] Banhart, F., Kotakoski, J., Krasheninnikov, A. V. (2011). Structural defects in graphene. *ACS Nano* 5, 26–41.
- [32] Trasatti, S. (1971). Work function, electronegativity, and electrochemical behaviour of metals: II. Potentials of zero charge and “electrochemical” work functions. *J. Electroanal. Chem. Int. Electrochem.* 33, 351–378.
- [33] Ringe, S., Hörmann, N. G., Oberhofer, H., Reuter, K. (2022). Implicit solvation methods for catalysis at electrified interfaces. *Chem. Rev.* 122, 10777–10820.
- [34] Kresse, G., Furthmüller, J. (1996). Efficiency of ab-initio total energy calculations for metals and semiconductors using a plane-wave basis set. *Comput. Mater. Sci.* 6, 15–50.
- [35] Kresse, G., Furthmüller, J. (1996). Efficient iterative schemes for ab initio total-energy calculations using a plane-wave basis set. *Phys. Rev. B* 54, 11169–11186.
- [36] Grau-Crespo, R., Hamad, S., Catlow, C. R. A., de Leeuw, N. H. (2007). Symmetry-adapted configurational modelling of fractional site occupancy in solids. *J. Phys.: Condens. Matter* 19, 256201.
- [37] Perdew, J. P., Burke, K., Ernzerhof, M. (1996). Generalized gradient approximation made simple. *Phys. Rev. Lett.* 77, 3865–3868.
- [38] Grimme, S., Antony, J., Ehrlich, S., Krieg, H. (2010). A consistent and accurate ab initio parametrization of density

- functional dispersion correction (DFT-D) for the 94 elements H-Pu. *J. Chem. Phys.* 132, 154104.
- [39] Grimme, S., Ehrlich, S., Goerigk, L. (2011). Effect of the damping function in dispersion corrected density functional theory. *J. Comput. Chem.* 32, 1456–1465.
- [40] Trucano, P., Chen, R. (1975). Structure of graphite by neutron diffraction. *Nature* 258, 136–137.
- [41] Sundararaman, R., Arias, T. A. (2013). Regularization of the Coulomb singularity in exact exchange by Wigner-Seitz truncated interactions: towards chemical accuracy in nontrivial systems. *Phys. Rev. B* 87, 165122.
- [42] Perdew, J. P., Burke, K., Ernzerhof, M. (1997). Generalized gradient approximation made simple [Phys. Rev. Lett. 77, 3865 (1996)]. *Phys. Rev. Lett.* 78, 1396.
- [43] Garrity, K. F., Bennett, J. W., Rabe, K. M., Vanderbilt, D. (2014). Pseudopotentials for high-throughput DFT calculations. *Comput. Mater. Sci.* 81, 446–452.
- [44] Letchworth-Weaver, K., Arias, T. A. (2012). Joint density functional theory of the electrode-electrolyte interface: application to fixed electrode potentials, interfacial capacitances, and potentials of zero charge. *Phys. Rev. B* 86, 075140.
- [45] Gunceler, D., Letchworth-Weaver, K., Sundararaman, R., Schwarz, K. A., Arias, T. A. (2013). The importance of nonlinear fluid response in joint density-functional theory studies of battery systems. *Modell. Simul. Mater. Sci. Eng.* 21, 074005.
- [46] Paek, E., Pak, A. J., Hwang, G. S. (2013). A computational study of the interfacial structure and capacitance of graphene in [BMIM][PF₆] ionic liquid. *J. Electrochem. Soc.* 160, A1–A10.
- [47] Lu, J., Bao, Y., Su, C. L., Loh, K. P. (2013). Properties of strained structures and topological defects in graphene. *ACS Nano* 7, 8350–8357.
- [48] Bhatt, M. D., Kim, H., Kim, G. (2022). Various defects in graphene: a review. *RSC Adv.* 12, 21520–21547.
- [49] Zhang, M. J., Deng, K., Wei, F., Wu, X. L., Du, L., Liu, W. (2022). Adsorption and desorption of tritium on/from nuclear graphite. *ACS Omega* 7, 752–760.
- [50] Rowe, P., Deringer, V. L., Gasparotto, P., Csányi, G., Michaelides, A. (2020). An accurate and transferable machine learning potential for carbon. *J. Chem. Phys.* 153, 034702.
- [51] Ugeda, M. M., Brihuega, I., Guinea, F., Gómez-Rodríguez, J. M. (2010). Missing atom as a source of carbon magnetism. *Phys. Rev. Lett.* 104, 096804.
- [52] Sepioni, M., Nair, R. R., Rablen, S., Narayanan, J., Tuna, F., Winpenny, R., Geim, A. K., Grigorieva, I. V. (2010). Limits on intrinsic magnetism in graphene. *Phys. Rev. Lett.* 105, 207205.
- [53] Wakabayashi, K., Yoshii, T., Nishihara, H. (2023). Quantitative study on catalysis of unpaired electrons in carbon edge sites. *Carbon* 210, 118069.
- [54] Denis, P. A., Iribarne, F. (2013). Comparative study of defect reactivity in graphene. *J. Phys. Chem. C* 117, 19048–19055.
- [55] Momma, K., Izumi, F. (2011). *VESTA 3* for three-dimensional visualization of crystal, volumetric and morphology data. *J. Appl. Crystallogr.* 44, 1272–1276.
- [56] Nishihara, H., Fujimoto, H., Itoi, H., Nomura, K., Tanaka, H., Miyahara, M. T., Bonnaud, P. A., Miura, R., Suzuki, A., Miyamoto, N., et al. (2018). Graphene-based ordered framework with a diverse range of carbon polygons formed in zeolite nanochannels. *Carbon* 129, 854–862.
- [57] Zhu, J. W., Mu, S. C. (2020). Defect engineering in carbon-based electrocatalysts: insight into intrinsic carbon defects. *Adv. Funct. Mater.* 30, 2001097.
- [58] Yu, Q. K., Jauregui, L. A., Wu, W., Colby, R., Tian, J. F., Su, Z. H., Cao, H. L., Liu, Z. H., Pandey, D., Wei, D. G., et al. (2011). Control and characterization of individual grains and grain boundaries in graphene grown by chemical vapour deposition. *Nat. Mater.* 10, 443–449.
- [59] Yu, W., Yoshii, T., Aziz, A., Tang, R., Pan, Z. Z., Inoue, K., Kotani, M., Tanaka, H., Scholtzová, E., Tunega, D., et al. (2023). Edge-site-free and topological-defect-rich carbon cathode for high-performance lithium-oxygen batteries. *Adv. Sci.* 10, 2300268.
- [60] Xia, T., Yoshii, T., Nomura, K., Wakabayashi, K., Pan, Z. Z., Ishii, T., Tanaka, H., Mashio, T., Miyawaki, J., Otomo, T., et al. (2023). Chemistry of zipping reactions in mesoporous carbon consisting of minimally stacked graphene layers. *Chem. Sci.* 14, 8448–8457.
- [61] Jänes, A., Eskusson, J., Thomberg, T., Lust, E. (2014). Electrochemical double layer capacitors based on propylene carbonate solution operating from –45°C to 100°C. *J. Electrochem. Soc.* 161, A712–A717.
- [62] Pohlmann, S., Balducci, A. (2013). A new conducting salt for high voltage propylene carbonate-based electrochemical double layer capacitors. *Electrochim. Acta* 110, 221–227.
- [63] Itoi, H., Nishihara, H., Kyotani, T. (2016). Effect of heteroatoms in ordered microporous carbons on their electrochemical capacitance. *Langmuir* 32, 11997–12004.
- [64] Jiang, H. R., Tan, P., Liu, M., Zeng, Y. K., Zhao, T. S. (2016). Unraveling the positive roles of point defects on carbon surfaces in nonaqueous lithium–oxygen batteries. *J. Phys. Chem. C* 120, 18394–18402.
- [65] Zhan, C., Neal, J., Wu, J. Z., Jiang, D. E. (2015). Quantum effects on the capacitance of graphene-based electrodes. *J. Phys. Chem. C* 119, 22297–22303.
- [66] Puschnig, P., Lüftner, D. (2015). Simulation of angle-resolved photoemission spectra by approximating the final state by a plane wave: from graphene to polycyclic aromatic hydrocarbon molecules. *J. Electron. Spectrosc. Relat. Phenom.* 200, 193–208.
- [67] Trasatti, S. (1986). The absolute electrode potential: an explanatory note (Recommendations 1986). *Pure Appl. Chem.* 58, 955–966.
- [68] Li, L., Reich, S., Robertson, J. (2005). Defect energies of graphite: density-functional calculations. *Phys. Rev. B* 72, 184109.
- [69] Kotakoski, J., Krasheninnikov, A. V., Kaiser, U., Meyer, J. C. (2011). From point defects in graphene to two-dimensional amorphous carbon. *Phys. Rev. Lett.* 106, 105505.

- [70] Błoński, P., Tuček, J., Sofer, Z., Mazánek, V., Petr, M., Pumera, M., Otyepka, M., Zbořil, R. (2017). Doping with graphitic nitrogen triggers ferromagnetism in graphene. *J. Am. Chem. Soc.* 139, 3171–3180.
- [71] Dideikin, A. T., Vul', A. Y. (2019). Graphene oxide and derivatives: the place in graphene family. *Front. Phys.* 6, 149.
- [72] Bakandritsos, A., Jakubec, P., Pykal, M., Otyepka, M. (2019). Covalently functionalized graphene as a supercapacitor electrode material. *Flatchem* 13, 25–33.
- [73] Nomura, K., Nishihara, H., Kobayashi, N., Asada, T., Kyotani, T. (2019). 4.4 V supercapacitors based on super-stable mesoporous carbon sheet made of edge-free graphene walls. *Energy Environ. Sci.* 12, 1542–1549.
- [74] Hahn, M., Baertschi, M., Barbieri, O., Sauter, J. C., Kötz, R., Gallay, R. (2004). Interfacial capacitance and electronic conductance of activated carbon double-layer electrodes. *Electrochem. Solid-State Lett.* 7, A33–A36.
- [75] Howell, J. O., Goncalves, J. M., Amatore, C., Klasinc, L., Wightman, R. M., Kochi, J. K. (1984). Electron transfer from aromatic hydrocarbons and their π -complexes with metals. Comparison of the standard oxidation potentials and vertical ionization potentials. *J. Am. Chem. Soc.* 106, 3968–3976.
- [76] De Waele, S., Lejaeghere, K., Sluydts, M., Cottenier, S. (2016). Error estimates for density-functional theory predictions of surface energy and work function. *Phys. Rev. B* 94, 235418.
- [77] Bramley, G., Nguyen, M. T., Glezakou, V. A., Rousseau, R., Skylaris, C. K. (2020). Reconciling work functions and adsorption enthalpies for implicit solvent models: a Pt (111)/water interface case study. *J. Chem. Theory Comput.* 16, 2703–2715.
- [78] Toh, C. T., Zhang, H. J., Lin, J. H., Mayorov, A. S., Wang, Y. P., Orofeo, C. M., Ferry, D. B., Andersen, H., Kakenov, N., Guo, Z. L., et al. (2020). Synthesis and properties of free-standing monolayer amorphous carbon. *Nature* 577, 199–203.
- [79] Simeral, L., Amey, R. L. (1970). Dielectric properties of liquid propylene carbonate. *J. Phys. Chem.* 74, 1443–1446.
- [80] Kislenko, V. A., Pavlov, S. V., Fedorov, M. V., Kislenko, S. A. (2021). New aspects of enhancing the graphene capacitance by defects in aqueous electrolytes and ionic liquids. *JETP Lett.* 114, 263–268.
- [81] Ando, Y., Gohda, Y., Tsuneyuki, S. (2013). *Ab initio* molecular dynamics study of the Helmholtz layer formed on solid-liquid interfaces and its capacitance. *Chem. Phys. Lett.* 556, 9–12.
- [82] Sruthi, T., Tarafder, K. (2019). Enhancement of quantum capacitance by chemical modification of graphene supercapacitor electrodes: a study by first principles. *Bull. Mater. Sci.* 42, 257.
- [83] Hassan, A., Mattioli, I. A., Colombo, R. N. P., Crespilho, F. N. (2023). Tuning quantum capacitance in 2D graphene electrodes: the role of defects and charge carrier concentration. *J. Mater. Chem. C* 11, 6301–6305.
- [84] Tang, R., Taguchi, K., Nishihara, H., Ishii, T., Morallón, E., Cazorla-Amorós, D., Asada, T., Kobayashi, N., Muramatsu, Y., Kyotani, T. (2019). Insight into the origin of carbon corrosion in positive electrodes of supercapacitors. *J. Mater. Chem. A* 7, 7480–7488.